Molecular-dynamics simulations of epitaxial crystal growth from the melt. II. Si(111)

W. D. Luedtke, Uzi Landman, M. W. Ribarsky, R. N. Barnett, and C. L. Cleveland
School of Physics, Georgia Institute of Technology, Atlanta, Georgia 30332
(Received 27 July 1987)

Molecular-dynamics simulations are employed in studies of liquid-phase epitaxial growth onto a Si(111) surface. The material is described using two- and three-body interaction potentials which provide a realistic description of crystalline silicon and of the crystal-melt interface. From equilibrium solid-melt coexistence, the system is driven out of equilibrium by allowing heat conduction to the underlying substrate. Two heat-extraction rates are used, resulting in growth velocities of 14 and 9 m/sec. The crystal grown under the faster growth conditions contains stacking faults, defective layers, and an amorphous region. The slower growth results in a more perfect crystal with stacking faults and a narrow region of disorder at the solid-vacuum interface. Crystallization is initiated when the crystal-melt interface supercools by ~ 150 K and a layer-by-layer growth mode is observed, accompanied by self-annealing processes. The dynamics of the crystal-growth processes are investigated with refined spatial and temporal resolution using real-space particle trajectories and following the evolution of the system temperature, potential-energy, and density profiles.

I. INTRODUCTION

Crystal growth from the melt by liquid-phase epitaxy (LPE) is one of the oldest methods for growing crystals.[1,2] The development of fast-pulsed-laser material-processing techniques, often called laser annealing, opens new avenues in crystal-growth technology and provides new ways and means for detailed studies of phase transformations and growth of material systems.[3–10] In particular, the development of time-resolved spectroscopic techniques and improved microscopy methods yield information on refined spatial and temporal scale which provide the impetus for the development of microscopic theoretical models of the physical processes which underlie phase-transformation and growth phenomena of materials. These developments, coupled with significant progress in the understanding of the nature of interactions and bonding in materials and in our computational capabilities, allow the formulation and implementation of computer simulations which are capable of providing realistic descriptions of material systems and of probing systematically the microscopic energetics and dynamics of processes in these systems.

In the first paper in this series[11] (see preceding paper, referred to as paper I), we have described in detail the development of computer molecular-dynamics (MD) simulations and their application to studies of LPE on the (001) surface of silicon. In this paper we employ the methods developed in paper I for studies of the dynamics of LPE on the (111) surface of silicon. Orientational dependencies of the growth mode and characteristics of the growth processes in LPE (such as the growth rates, the types of defects and their generation mechanisms, and the threshold interface velocity for amorphization) have been observed even at the high growth velocities occurring in pulsed-laser experiments.[12–15,10] In addition, the orientational dependence of the growth velocity has been discussed in the context of Monte Carlo calculations based on a kinetic Ising model[16] of the crystal-melt interface and MD simulations of face-centered-cubic material employing Lennard-Jones (LJ) potentials.[17–20] Also, orientational dependencies of the diffuse structure and extent of the equilibrium solid-melt interface have been found using MD simulations employing LJ potentials[17,19,21] and more recently in simulations[22,23] employing two- and three-body interactions constructed[24] and parametrized to adequately describe the properties of tetrahedrally bonded materials, Si in particular. In these later studies it was found that the coexistence crystal-melt interfaces of Si(001) and Si(111) differ markedly. While the Si(111) crystal-melt equilibrium interface is characterized by a sharp, abrupt and flat transition from the crystal to the melt region, the interface for the (001) orientation is broad and structured, exhibiting a pronounced tendency for the formation of microfacets based on (111) planes.[22] In addition, the melt region in the vicinity of the solid-melt interface exhibits for both orientations a certain degree of ordering due to the underlying crystalline potential, resulting in a diffuseness of the interface at that region. As discussed in paper I (Ref. 11) molecular-dynamics simulations are ideally suited for studies of LPE since, by following the time evolution of all particles of the system, the dynamics of the two phases (solid and liquid) comprising the system is included. Thus cooperative dynamical effects (particularly of importance in the liquid) as well as the energies of the system and interfacial kinetics are treated in these simulations on equal footing, unlike kinetic models where only the latter effects are considered.

Starting from an equilibrated system at solid-melt coexistence, with a (111) interface, we have investigated liquid-phase-epitaxial growth which was driven by allowing heat conduction to the substrate. In these investigations we have employed the same procedure of sample preparation and growth simulation as in our studies of LPE on the (001) surface (see paper I). Using the same

 ©1988 The American Physical Society

cooling rate as the one used for the (001) surface, growth occurred at a velocity of 14 m/sec, yielding a grown crystal which contained an assortment of defects (stacking faults, in-layer defects, and a disordered region). Reducing the cooling rate by a factor of $\frac{1}{2}$ resulted in a growth velocity of 9 m/sec, with the grown crystal possessing a markedly higher degree of perfection (stacking faults and a very narrow region of disorder limited to the crystal-vacuum interface). In the following we refer to these two simulations as the fast and slow studies, respectively. As in the case of the (001) system we find for both cooling rates of the (111) system that crystallization did not start until the temperature at the interface dropped from the initial-melting-point temperature by about 150 K. Once crystallization starts the crystal-melt interface propagates by a layer-by-layer growth mode, with the interface maintaining a sharp character. We find, however, that unlike growth on the (001) surface which occurred in an almost continuous, monotonous, manner, the advance of the crystallization front versus time in both (111) systems is discontinuous, with periods of crystallization interrupted by stages of no apparent forward movement of the interface. Close inspection reveals that during these stages self-annealing of defects occurs. As the defective region achieves a high level of structural perfection, crystallization resumes.

Following a brief description of the setup of the system we describe in the next section our results of LPE on the (111) surface of silicon, and discuss them in light of experimental observations.

II. LIQUID-PHASE EPITAXY ON Si(111)

The simulation system is constructed as a thick slab which is periodically repeated in two directions and is free, with no imposed boundary condition, in the third direction. Additionally, it is positioned on top of a static substrate, composed of four layers, which is set up in [111] orientation with the Z axis parallel to the [111] crystallographic direction and the two-dimensional (2D) cell is defined by the $[\bar{1}10]$ and $[10\bar{1}]$ directions. The number of layers, N_L, in the initial crystalline system (which was then partially melted via a heat pulse, as described in paper I) was 20 with 49 particles per layer (i.e., the total number of dynamic particles was 980). In the numerical integration of the equations of motion, using a fifth-order predictor-corrector algorithm, we employed a time step $\Delta t = 1.15\times10^{-3}$ psec; with this choice and a frequent updating of the interaction lists (every $8\Delta t$), the total energy of the system is conserved to at least six significant figures (for a few thousand time steps). All other technical details of the simulation and the interaction potentials are as described for the (001) system in paper I (see Sec. II of I). Throughout, energy and temperature are expressed in units of $\varepsilon = 50$ kcal/mol (to convert to temperature in K, multiply the reduced temperature by 2.517×10^4) and length in units of $\sigma = 2.0951$ Å.

Starting from an equilibrated crystalline sample[22] at $T = 0.064$ (1593 K), a heat pulse was applied (via scaling of velocities) to the top $\frac{1}{3}$ of the system and the system was allowed to evolve for 1.5×10^5 time steps (~ 175 psec), yielding an equilibrated system at solid-melt coexistence at $T_m = 0.0670\pm0.0020$ (1685 K). Particle trajectories (recorded for $2000\Delta t$) viewed along the $[1\bar{1}0]$ direction and in-layer trajectories for layers 10, 11, and 8,9 are shown[22] in Figs. 1(a), 1(b), and 1(c), respectively, along with the density, Fig. 1(d), and per-particle potential-energy profiles, Fig. 1(e), in the [111] direction (with $Z^* = 1 \equiv 14.96\sigma$, where $\sigma = 2.0951$ Å, and the unit of length in the $[1\bar{1}0]$ and $[10\bar{1}]$ directions is 12.85σ). As is evident from the figure, the solid-melt interface is sharp, abrupt, and flat [to be contrasted with the broad, structured interface found for the equilibrium solid-melt interface of the (001) system;[22] see Fig. 2 of paper I]. Additionally, it is seen that though layer 10 is clearly identifiable in the particle density profile, particles in this region exhibit a partial liquidlike characteristic, as is evident from the particle trajectories [Fig. 1(b)] and the high value of the three-body potential energy [Fig. 1(e)] at the location corresponding to the occurrence of the layer in the density profile.

Having obtained an equilibrium system, the growth simulations were initiated by extracting heat from the system via scaling of particle velocities in the bottom two layers, as described in paper I. Two simulation experiments were performed: one in which the rate of heat extraction was as that used for the (001) system (i.e., scaling of velocities every $5\Delta t$ such as to remove at a constant rate an amount of energy which is equal to the latent heat per layer every 6 psec), and the other where half the above rate was used (the "fast" and "slow" simulations, respectively).

The time evolutions of the overall system temperature and of the three- and two-body contributions to the potential energy of the system are shown in Figs. 2 and 3 for the "fast" and "slow" simulations, respectively. In both

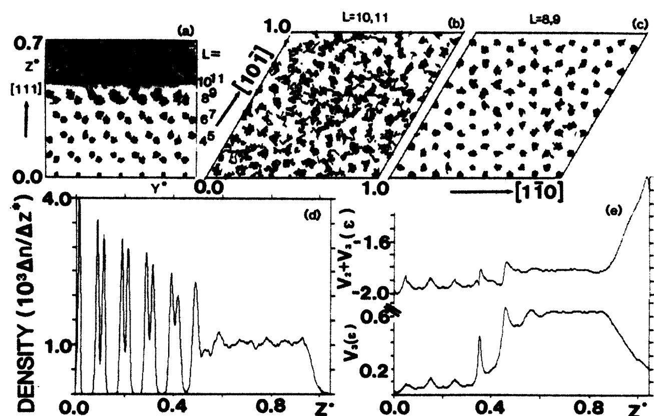

FIG. 1. (a) Particle trajectories recorded at equilibrium, viewed along the $[1\bar{1}0]$ direction (Ref. 22) (b) and (c) In-plane trajectories, exhibiting melt and solid characteristics, in layers 10, 11, and 8,9, viewed along the [111] Z^* direction. $Z^* = 1 \equiv 14.9\sigma$ and the unit of length in the $[1\bar{1}0]$ and the $[10\bar{1}]$ directions is 12.85σ. (d) Equilibrium particle density, $\Delta n/\Delta Z^*$, vs Z^*. (e) Per-particle total and three-body potential energies V_2+V_3 and V_3 vs Z^*.

cases, in the initial stage of the simulation the system temperature drops continuously, as a result of the heat conduction to the substrate, with no significant ordering observed. Once the temperature has dropped to a certain level (see below), crystallization is initiated, as noted in the figures ($\sim$43 and 58 psec for the fast and slow systems, respectively). The time developments of both systems exhibit a characteristic nonmonotonous behavior (particularly pronounced in the potential energies [Figs. 2(b) and 2(c), and 3(b) and 3(c)]. This behavior should be contrasted with the monotonous, continuous changes found for the (001) system (see paper I, Fig. 3), and is due to differences in the growth modes for these two crystalline orientations. As we discussed above, the Si(111) solid-melt interface is structurally different and less complex than that for the Si(001) system, exhibiting a flat morphology. In addition, in the present system the influence of the crystalline potential on the melt adjacent to it extends over a rather narrow region, resulting in a more abrupt interface. These characteristics pertain not only to the equilibrium state but maintain during growth. As a result, growth on the (111) surface occurs in a layer-by-layer manner. The above-mentioned discontinuities in the growth rate are related to the ordering processes in each of the added layers. An additional effect characteristic to the (111) system is seen at $\sim$70 psec for the fast system (Fig. 2) and $\sim$140 psec for the slow one (Fig. 3), where a marked change in the rate of crystallization occurs, accompanied by a period of almost constant temperature. As we discuss below this effect is associated with self-annealing processes and subsequent fast growth.

In Figs. 4 and 5 profiles of the system temperature (in units of $\varepsilon = 50$ kcal/mol) versus Z^* ($Z^* = 1 = 14.96\sigma$) at selected times are shown, for the fast and slow simulation, respectively. These profiles were obtained as short-time averages ($2\times10^3\Delta t$) and therefore they exhibit a degree of noise. In both systems we observe that during the initial cooling period preceding crystallization the temperature drops throughout the system below the initial-($t=0$) melting-point temperature. Crystallization starts ($t=43$ psec in Fig. 4 and 58 psec in Fig. 5) when the temperature at the solid-melt interface drops to $\lesssim 0.06$, which corresponds to an undercooling of ≥ 150 K.

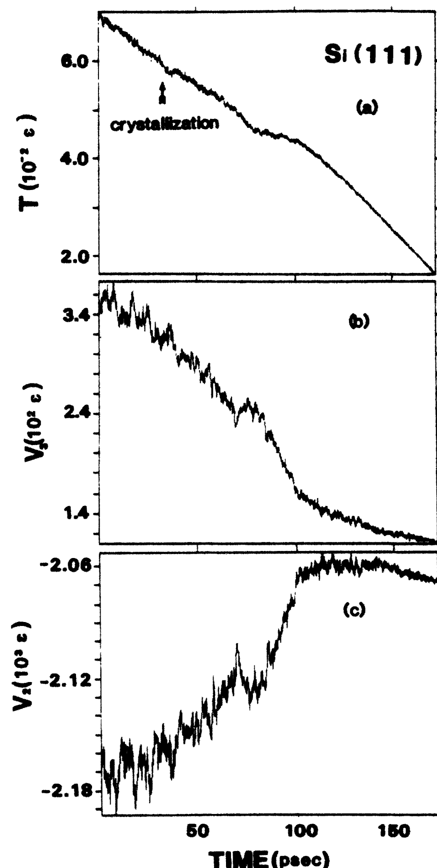

FIG. 2. Time development of the system temperature, T, in units of ε ($\varepsilon = 50$ kcal/mol) and of the per-particle three- and two-body contribution to the potential energy throughout the growth simulation of the "fast" heat-extraction system, starting from the beginning of the heat extraction at $t=0$. The start of the crystallization stage is noted ($\sim$43 psec). Note the nonmonotonous character of the process.

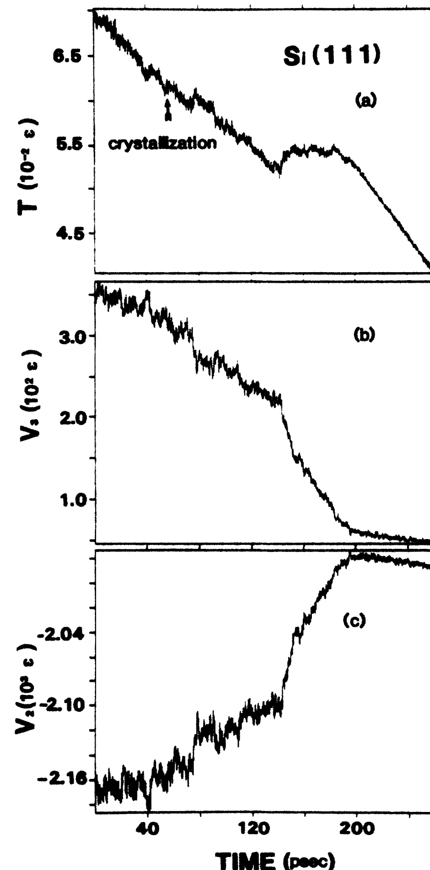

FIG. 3. Same as Fig. 2, for the "slow" heat-extraction system. The start of the crystallization stage is noted ($\sim$58 psec). Note the nonmonotonous character of the process.

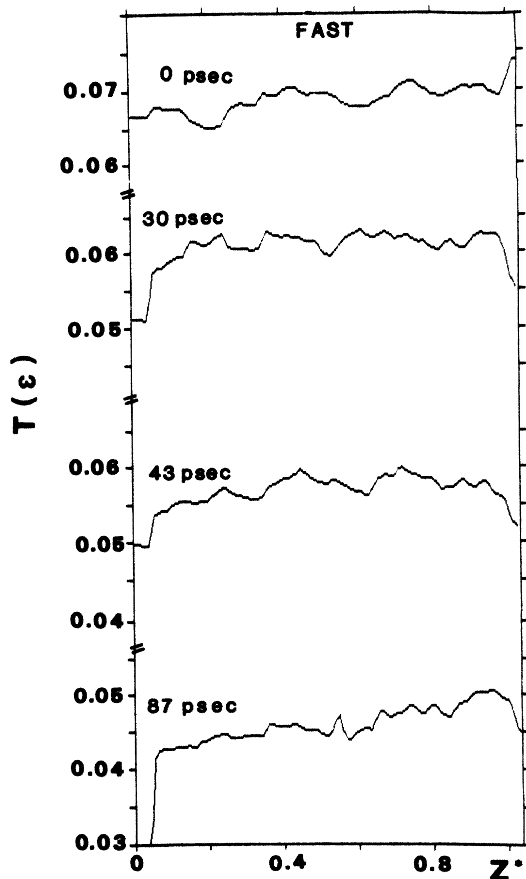

FIG. 4. Temperature, T, profiles at selected times during the simulation of the "fast" Si(111) system. The $t=0$ profile was recorded for the equilibrium solid-melt coexistence system. All profiles were obtained as short-time averages over $2\times10^3\Delta t$.

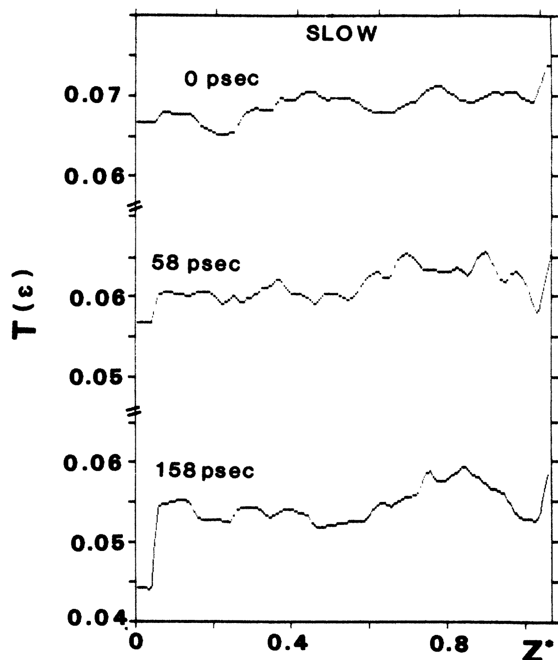

FIG. 5. Same as Fig. 4, for the "slow" Si(111) system.

In the following we present first the results for LPE under high-velocity growth conditions, followed by those for the slower-velocity growth.

A. High-velocity growth

In order to investigate the details of the growth process, we present in Figs. 6–8 profiles of the particle densities, $\Delta n/\Delta Z^*$ versus Z^* along the [111] direction. In order to illustrate the evolution of the energetics of the system, we show also for the time period 0–58 psec (Figs. 6 and 7) profiles of the per-particle potential energy, V_2+V_3, and those for the individual contributions, V_2 and V_3, recorded at selected times during the simulation. Since the system is in a nonequilibrium state, dynamically evolving in time, these profiles were obtained as short-time averages ($\sim10^3\Delta t$) and therefore they contain a degree of noise. We were forced, however, to employ such short averaging times in order to capture the temporal characteristics of the system at selected times during the

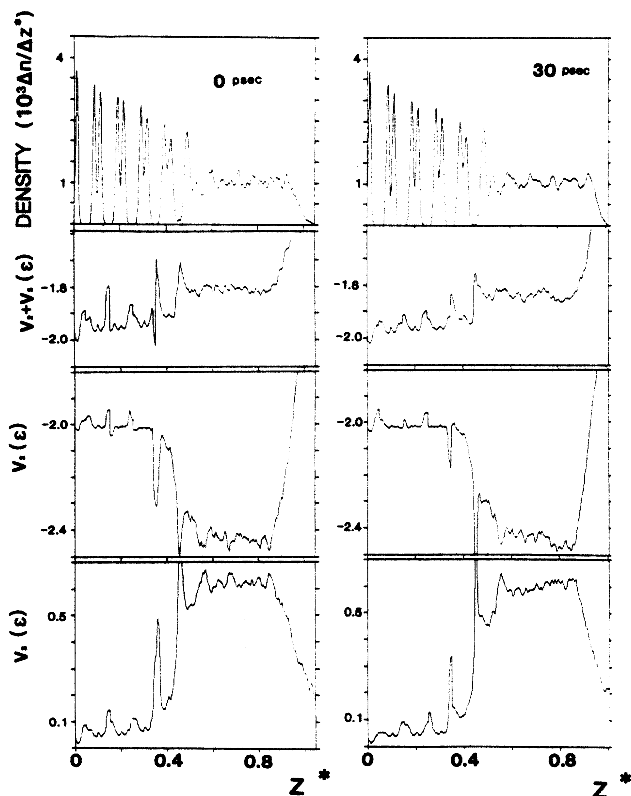

FIG. 6. Profiles of the particle density $\Delta n/\Delta Z^*$, where Δn is the number of particles with Z^* coordinates between Z^* and $Z^*+\Delta Z^*$, and profiles of the per-particle total potential energy, V_2+V_2, and of the two- and three-body contributions (V_2 and V_3, respectively) vs Z^* ($Z^*=1\equiv14.96\sigma$), at $t=0$ and 30 psec for the "fast" Si(111) system. In the crystalline region, maxima in the density profiles and the corresponding minima in the potential-energy profiles occur at the crystalline layer positions. Comparison of the profiles for the two times demonstrates that no significant crystallization occurred during the initial cooling stage.

growth process. Thus, while in the solid region the pronounced maxima in the density profiles and the corresponding minima in the potential energies occur at the locations of crystalline layers, occasionally the random displacement of a small number of particles into the spacing between crystalline layers shows up in the potential-energy profiles as spikes (whereas inspection of the density profile at those locations indicates good crystalline order). No such occurrences are seen in the liquid region since, even for the short averaging times which we used, the diffusion of particles in the melt averages out such spurious features.

Inspection of the profiles shown in Fig. 6 at $t=0$ and 30 psec reveals that during this time period no crystallization occurred. From Figs. 4 and 2 we observe that during this time period the temperature of the system drops to a little over 0.06. As seen from Figs. 4 (compare the temperature profiles at 30 and 43 psec) and 2, the temperature continued to decrease to below 0.06 (a supercooling of over 150 K). Concomitant with this degree of supercooling [similar to that found in the Si(001) system at the final stages of the cooling period], we observe by comparing the profiles at $t=43$ psec shown in Fig. 7 to those at $t=30$ psec that growth started to occur, and the interface advanced by that time by adding at least one crystalline layer to the solid (note the drops in the values of V_3 at the locations of layers 11 and 12 in the corresponding density profile). During the subsequent 15 psec an additional layer (number 13) starts to grow and a refinement of the structure of the neighboring underlying crystalline region occurs, as the $t=58$ psec profiles in Fig. 7 demonstrate. At this time the advance of the crystallization front slows significantly as evident from the profiles shown in Figs. 8(a) and 8(b) at $t=72$ and 87 psec, respectively. In contrast, in the time period between 87 and 101 psec [see Fig. 8(c)], growth resumes with the addition of 2–3 layers at the latter time.

A closer look at the evolution of the system between $t=58$ and 101 psec is provided by the real-space particle trajectories, viewed along the $[1\bar{1}0]$ direction, and in-layer trajectories for layers 10–13, shown in Fig. 9. Comparison of the position of the interface, in the top of the figure, for $t=58$, 72, and 87 psec indicates that it did not advance during this time period. The in-layer parti-

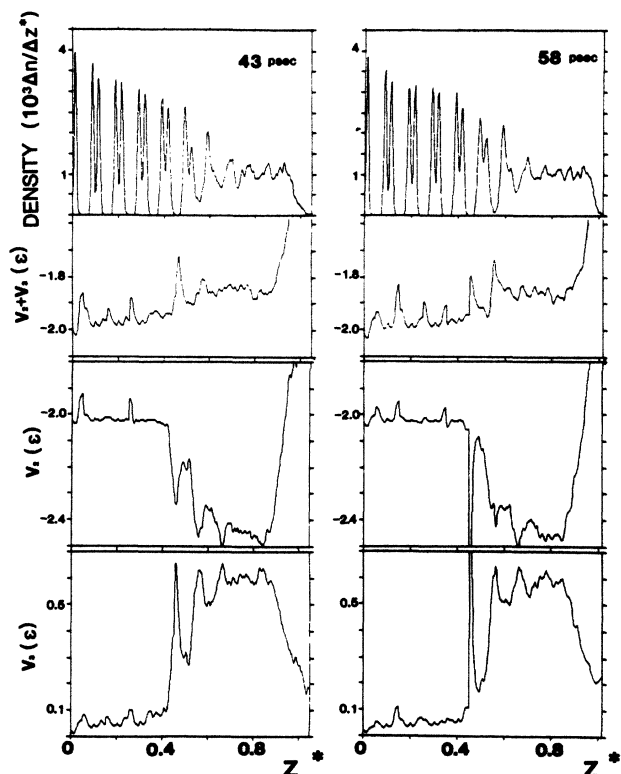

FIG. 7. Same as Fig. 6 for $t=43$ psec (start of the crystallization stage; see Fig. 2) and $t=58$ psec. Comparison of the profiles at the two times demonstrates growth.

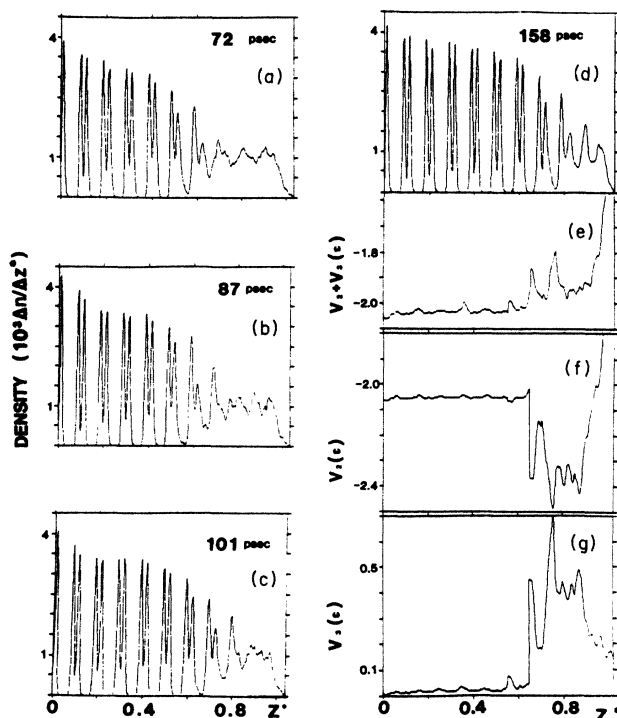

FIG. 8. Profiles of the particle density $\Delta n/\Delta Z^*$, where Δn is the number of particles with Z^* coordinate between Z^* and ΔZ^* for the "fast" growth simulation at (a) $t=72$ psec, (b) $t=87$ psec, (c) $t=101$ psec, and toward the end of the simulation at (d) $t=158$ psec. Comparison of the profiles at $t=58$ psec (Fig. 7) and those recorded in the time span 72–87 psec [panels (a) and (b)] demonstrates the interruption in the advance of the crystallization during this time period (see also the temperature and potential energy for the system, during this time, shown in Fig. 2). Comparison of the profile at $t=101$ psec [panel (c)] to those at earlier times [panels (a) and (b)] demonstrates the resumption of the solid-melt interface propagation. For the final state of the system ($t=158$ psec) we also show profiles of the potential energies [panels (e) and (f)], demonstrating the degree of imperfection of the grown crystal (note, in particular, the high values of V_3 for $Z^*>0.7$).

cle trajectories at $t=58$ psec reveal a defective region in crystalline layer 10 (see lower left-hand portion), which induces a similar defective region in layer 11 above it. These defects persist at a later time ($t=72$ psec), until at $t=87$ psec they are annealed (note the constancy of V_3 during this time period, in Fig. 2). Once the in-layer defect was annealed vigorous growth resumed, as is evident from the trajectories shown for $t=101$ psec (see also Fig. 2). This sequence of events demonstrates an interesting phenomena of *dynamical self-annealing* in which the evolving system self-corrects structural errors, thus improving the quality of the grown crystal. We also found evidence for this mechanism in the simulation of the slow-growth-velocity system.

Views of the system towards the end of the simulation are given by the profiles in Fig. (8) ($t=158$ psec) and the real-space particle trajectories, viewed along the $[1\bar{1}0]$ direction in Fig. 10. From the original location of the solid-melt interface and the final location of the top of the grown crystal and the time which lapsed between these two states, we estimate the growth velocity as ~ 14 m/sec.

The structure of the grown crystal (see Fig. 10) reveals a crystalline region with perfect intralayer order, but containing "mistakes" in the registry of layers (stacking faults), as well as a region of defective layers and a wide region of a disordered solid, closer to the solid-vacuum interface. The imperfection of the grown crystal is reflected also in the potential-energy profiles shown in Figs. 8(e) and 8(f), at $t=158$ psec, towards the end of the simulation. We also note that towards the end of the simulation the temperature of the system dropped significantly, such that activation barriers for defect annealing and disorder-order transformations cannot be surmounted. As will be shown below, the structural quality of the grown crystal is dramatically improved upon reducing the growth velocity.

B. Low-velocity growth

We turn now to presentation of the results for the slow-rate-of-growth system. As indicated in Fig. 3 in the first stage after the start of the heat conduction to the substrate, the system undercools with no significant growth occurring. The temperature profiles shown in Fig 5 demonstrate that by 58 psec the temperature at the interface region dropped to $\lesssim 0.06$, and, as an inspection of the density and potential-energy profiles shown in Fig. 12

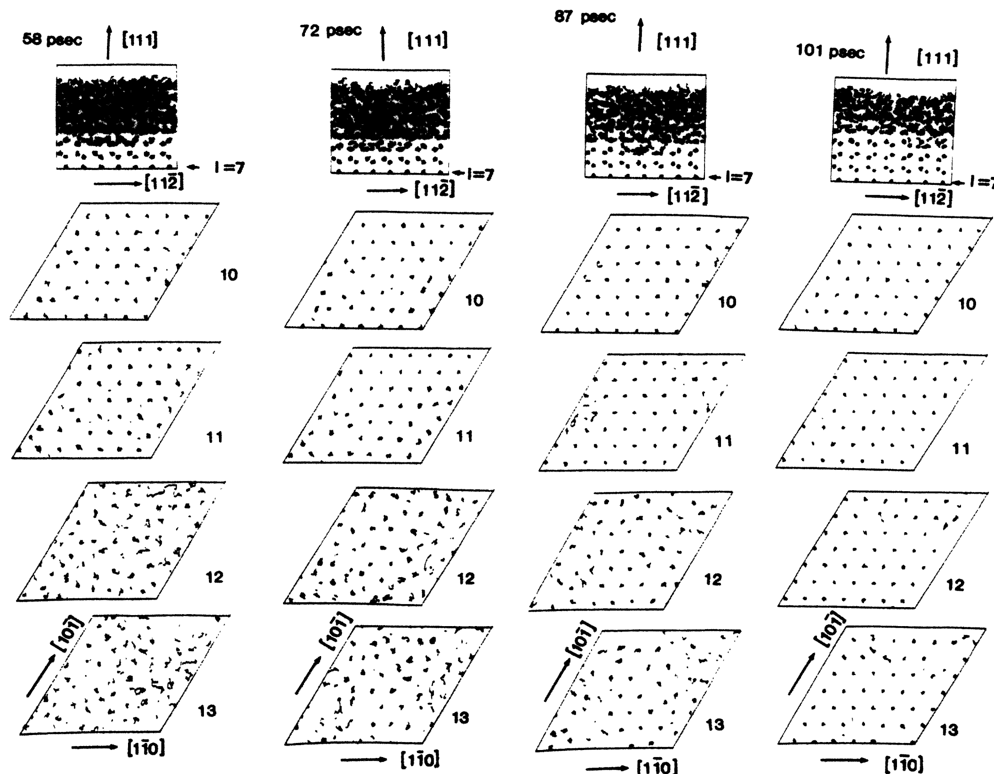

FIG. 9. Top: real-space particle trajectories, viewed along the $[1\bar{1}0]$ direction, recorded at the denoted times (58–101 psec) during the simulation of the "fast" Si(111) system. Comparison of the real-space trajectories at these times demonstrates the interruption in the crystallization front advance during $t=58-87$ psec and the resumption of progress at 101 psec. Bottom: in-layer particle trajectories at the corresponding times (recorded for $10^3\Delta t$). Note the defect (located at the lower left) in layer 10 at $t=58$ and 72 psec, which induces the occurrence of a defective region above it, in layer 11, at these times. By $t=87$ psec, the defective region in layer 10 was annealed as was layer 11, inducing a higher degree of order in layers 12 and 13. By $t=101$ psec all four layers exhibit perfect in-layer crystalline order. This sequence demonstrates a self-annealing process.

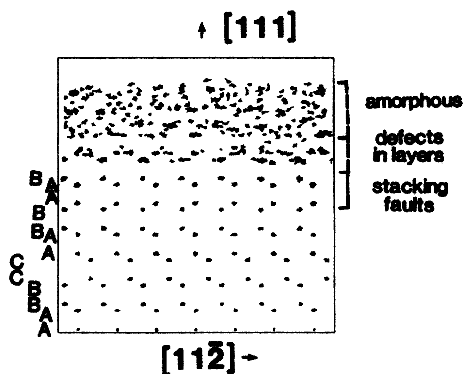

FIG. 10. Real-space particle trajectories of the fast Si(111) system, viewed along the $[1\bar{1}0]$ direction, at the end of the simulation. The grown crystal contains stacking faults, defective crystalline layers, and an amorphous region. The distance from bottom to top of the inscribed boundaries is $14.96\sigma = 31.34$ Å.

indicates, by about that time growth has begun. We note from the temperature profile in Fig. 5 ($t = 58$ psec) that crystallization in this system occurs while the temperature in the melt region ($Z^* > 0.6$) is higher than in the crystalline part. Comparison of the profiles at 58 psec (Fig. 11) and those recorded about $t = 72$ psec demonstrates the slow growth [Fig. 12(a)]. We also observe that

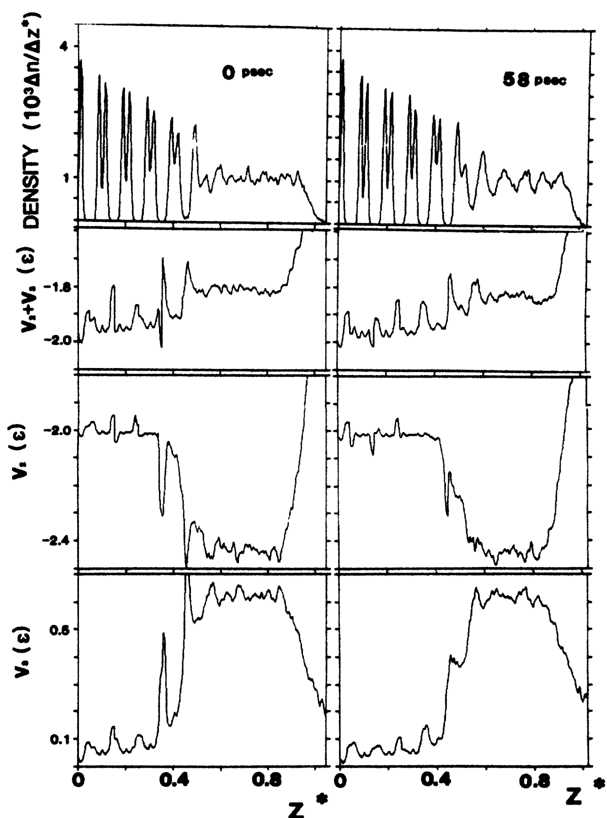

FIG. 11. Particle density and potential-energy profiles for the "slow" Si(111) system at equilibrium $t = 0$, and at $t = 58$ psec, shortly after the beginning of the crystallization process.

during the next 72 psec only about one additional layer grew. At about $t = 144$ psec radical changes in the rates of variation of the overall system temperature and potential energies are evident (see Fig. 3). The constancy of the temperature starting at about that time and sharp drops in V_3 and V_2 signify growth at a much faster rate than before that time as is evidenced by comparing the density and potential-energy profiles for $t = 158$ psec in Fig. 12(c) with those at $t = 144$ psec [Fig. 12(b)]. From the temperature profile of the system at $t = 158$ psec (see Fig. 5), during the growth period we observe that the faster progress of the crystallization front occurs when the interface region is at a temperature of ~ 0.058, while the crystalline material is at a lower temperature, thus forming a gradient.

The final stages of the simulation are described by the profiles at $t = 259$ psec [Fig. 12(d)] and the real-space par-

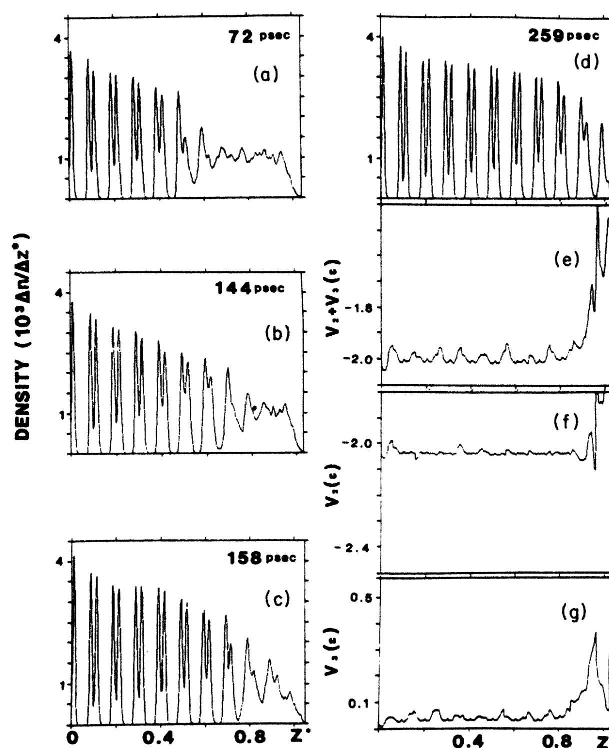

FIG. 12. Particle density profiles for the "slow" Si(111) system at (a) $t = 72$ psec, (b) $t = 144$ psec, (c) $t = 158$ psec, and (d) $t = 259$ psec. Comparison of the profile at $t = 72$ [panel (a)] and 58 psec (Fig. 11), shows an interruption of the advancement of the crystallization front. The slow growth occurring between 72 and 144 psec is demonstrated via comparison of the profiles for these times [panels (a) and (b)]. At $t = 144$ psec, a fast growth stage occurs as evidenced by inspection of the profiles for $t = 158$ and 259 psec (see also the sharp drop in V_3 and V_2, and the constant temperature period in Fig. 3, starting at $t \approx 145$ psec). For the final state of the system ($t = 259$ psec) we show also profiles of the potential energies [panels (e) and (f)]. Comparison of these profiles with those for the "fast" growth system at the end of the simulation [Figs. 8(e) and 8(f)] demonstrate the higher degree of perfection of the grown crystal obtained via the "slow" growth process.

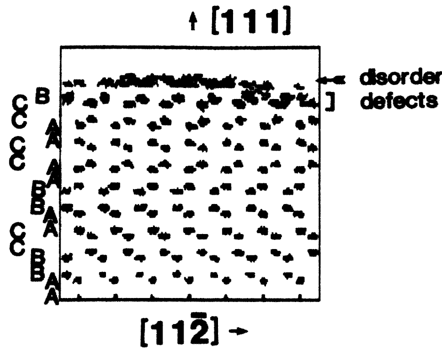

FIG. 13. Real-space particle trajectories of the slow Si(111) system, viewed along the [1$\bar{1}$0] direction, at the end of the simulation. The grown crystal shows a high degree of structural perfection. It contains stacking faults and a narrow region of inlayer defects and disorder, limited to the immediate solid-vacuum interface.

ticle trajectories, viewed along the [1$\bar{1}$0] direction, shown in Fig. 13. From Fig. 13 we conclude that at the present growth velocity, estimated as $\sim$9 m/sec, a crystal possessing a high degree of structural perfection was grown. We observe in it stacking faults and a very narrow band of defective layers and disorder limited to the immediate vicinity of the solid-vacuum interface. The high degree of perfection obtained in this system is also evidenced by inspection of the potential-energy profiles at the end of the process [Figs. 12(e) and 12(f)], exhibiting low values of V_3 and the total potential energy up to the vicinity of the solid-vacuum interface.

III. DISCUSSION

In this paper [and in paper I (Ref. 11)] we have developed a methodology for molecular-dynamics studies of equilibrium and nonequilibrium interfaces and have employed it in investigations of liquid-phase-epitaxial growth of silicon on the (111) and (001) surfaces, using interaction potentials which include two and three-body contributions and provide an adequate description of the material. As discussed and demonstrated in paper I, growth on the (001) surface at high interface velocity ($\sim$18 m/sec) involved an undercooled, structured, microfaceted solid-melt interface and proceeds in a continuous, monotonous manner, yielding a structurally perfect grown crystal. Comparison of our results for the two surfaces highlights the orientational dependence of the growth processes, which was experimentally observed,[10,12–15] and provides insights into the nature of liquid-phase epitaxy. As discussed in paper I (see Sec. IV of that paper), it is pertinent to discuss the results of our studies in light of the information obtained in laser-annealing experiments.

In the first stage of our simulations a system at equilibrium, solid-melt coexistence at the melting point was prepared. The melting point of the system was determined to be 0.067$\pm$0.0020 (1685 K), in good agreement with the experimental melting point of Si (1683 K). The latent heat which we estimated from the difference of the average potential energies in the solid and melt region is 31.4 kJ/mol, compared to the experimental value of 50.7 kJ/mol. The solid-melt interface in equilibrium is characterized as sharp, abrupt, and flat, in contrast to the microfaceted, broad, structured interface found for the equilibrium interface of the (001) system.[11]

Starting from the equilibrium state, the system was cooled by extracting energy from the bottom two layers of the dynamical system, which are sufficiently removed from the interface region such that the effect of heat extraction (via scaling of velocities every $5\Delta t$) does not interfere with the dynamical evolution of the system in that region. As described in the preceding section, two rates of cooling were employed. In the "fast" rate simulations, which resulted in a growth velocity of $\sim$14 m/sec, the constant rate of heat extraction was 61.25 kcal/mol psec, and in the "slow" simulations, resulting in a growth velocity of 9 m/sec, the cooling rate was 30.625 kcal/mol psec. These rates of energy removal correspond to cooling rates of $\sim 2\times 10^{12}$ and $\sim 1\times 10^{12}$ K/sec, respectively. We note that these cooling rates are in the range of values which may be achieved in laser-annealing experiments.[15] As in the case of the (001) system,[11] in the initial stage after heat conduction to the substrate started, the temperature of the system drops with no discernable crystallization observed. In both the "fast" and "slow" cooling simulations, ordering and crystallization began only when the overall system temperature dropped below the melting point, and the supercoolings in the interface regions were $\geq$200 and $\sim$150 K, respectively (see Figs. 4 and 5). These degrees of supercooling are similar to that which we found for the (001) system [for the "fast" system, which was cooled at the same rate as the (001) system, the observed supercooling is somewhat higher]. The crystallization which ensued past the initial cooling stage, for both cooling rates, is characterized as discontinuous (nonmonotonous) with periods of rapid crystallization interrupted by stages of cessation of the propagation of the interface. This behavior, which contrasts with the monotonous growth rate in the (001) system, indicates a difference in the growth modes for these two crystalline orientations. The flat, abrupt, solid-melt interface in the (111) system maintains during growth. Since in this system the spatial variation of the crystalline potential extends over a rather narrow region, it affects only the melt particles in its immediate vicinity and growth occurs via a layer-by-layer mechanism. Furthermore, we have found that growth is accompanied by dynamical self-annealing processes which provide a mechanism for structural perfection. We observed that occasionally propagation of the crystallization front is halted and then is resumed after a certain period of time ($\sim$30–50 psec). Closer inspection reveals that these events are related to the occurrence of defects in a newly crystallized layer which then induce the generation of defects in the subsequent crystallizing layers above it. The proliferation of these defects stops further motion of the interface. During the halting period annealing processes take place. Once the structural perfection has been restored, vigorous crystallization resumes. These self-annealing pro-

cesses are characteristic of the (111) system and are connected with the ease with which defects can occur in this system as compared with that for the (001) orientation [related to the smoothness of the interface and the fact that Si(111) requires the formation of triple and single bonds]. We also find that such self-annealing processes become more predominant at high growth velocities. In this context we note that, for the same cooling rate, growth on the (001) system proceeded at a higher rate (~ 18 m/sec) than on the (111) system (~ 14 m/sec, obtained in the "fast" simulations) in agreement with observations[12–14] and previous theoretical studies.[16] Moreover, unlike the case for the (001) system, the crystal grown on the (111) surface at high velocity is imperfect, containing stacking faults, defective layers, and a wide region of disordered material. We note that the mistakes in registry (stacking faults) involve perfectly ordered layers and occur closer to the start of the crystallization stage than the generation of defective layers and disordered region, which start to occur only later, after the temperature of the system drops significantly and activation barriers for defect self-annealing cannot be surmounted. The perfection of the grown crystal is markedly improved by reducing the cooling rate, resulting in a lower growth velocity (~ 9 m/sec) and yielding a grown crystal containing stacking faults and only a narrow region of disorder, limited to the immediate vicinity of the solid-vacuum interface. These observations correlate well with experimental observations[12–15] (see, in particular, Ref. 13) and provide a microscopic understanding of the nature and mechanisms of epitaxial growth.

ACKNOWLEDGMENTS

This work was supported by the U.S. Department of Energy under Grant No. FG05-86ER45234 and in part by a grant from the North American Philips Corporation. The computations were performed on the Cray-XMP computer at the National Magnetic Fusion Energy Computer Center, Livermore, California.

[1] *Crystal Growth and Materials,* Vol. 2 of *Current Topics in Material Science,* edited by E. Kaldis and H. J. Scheel (North-Holland, Amsterdam, 1977).

[2] *Crystal Growth: A Tutorial Approach,* edited by W. Bardsley, D. T. J. Hurle, and J. B. Mullin (North-Holland, Amsterdam, 1979).

[3] *Laser-Solid Interactions and Laser Processing–1978 (Materials Research Society, Boston),* proceedings of the Symposium on Laser-Solid Interactions and Laser Processing, AIP Conf. Proc. No. 50, edited by S. D. Ferris, H. J. Leamy, and J. M. Poate (AIP, New York, 1979).

[4] *Laser and Electron-Beam Interactions with Solids,* edited by B. R. Appleton and G. K. Celler (North-Holland, Amsterdam, 1982).

[5] *Laser-Solid Interactions and Transient Thermal Processing of Materials,* edited by J. Narayan, W. L. Brown, and R. A. Lemons (North-Holland, Amsterdam, 1983).

[6] *Energy Pulse Modifications of Semiconductors and Related Materials,* edited by K. Hennig (Akademie der Wissenschaften der DDR, Rossendorf, 1984), Vols. 1 and 2.

[7] *Laser Annealing of Semiconductors,* edited by J. M. Poate and J. W. Mayer (Academic, New York, 1982).

[8] *Pulsed Laser Processing of Semiconductors,* Vol. 23 of *Semiconductors and Semimetals,* edited by R. F. Wood, C. W. White, and R. T. Young (Academic, Orlando, 1984).

[9] See review by K. A. Jackson, in *Surface Modification and Alloying,* edited by J. M. Poate, G. Foti, and D. C. Jacobson (Plenum, New York, 1983), Chap. 3.

[10] See review by J. M. Poate, J. Cryst. Growth **79**, 549 (1986).

[11] U. Landman, W. D. Luedtke, M. W. Ribarsky, R. N. Barnett and C. L. Cleveland, preceding paper, Phys. Rev. B **37**, 4637 (1988).

[12] See review by A. G. Cullis, in *Laser Annealing of Semiconductors,* Ref. 7, Chap. 6, p. 147; C. W. White, B. R. Appleton, and S. R. Wilson, *ibid.,* Chap. 5, p. 111; C. W. White, in *Pulsed Laser Processing of Semiconductors,* Ref. 8, Chap. 2, p. 43; J. M. Poate, Mater. Res. Soc. Symp. Proc. **4**, 121 (1982).

[13] A. G. Cullis, N. G. Chew, H. C. Weber, and D. J. Smith, J. Cryst. Growth **68**, 624 (1984).

[14] A. G. Cullis, H. C. Weber, N. G. Chew, J. M. Poate, and P. Baeri, Phys. Rev. Lett. **49**, 219 (1982).

[15] R. Tsu, R. T. Hodgson, T. Y. Yan, and J. E. E. Baglin, Phys. Rev. Lett. **42**, 1358 (1979).

[16] G. H. Gilmer, in *Laser-Solid Interactions and Transient Thermal Processing of Materials,* Ref. 5, p. 249.

[17] U. Landman, C. L. Cleveland, and C. S. Brown, Phys. Rev. Lett. **45**, 2032 (1980); U. Landman, C. L. Cleveland, C. S. Brown, and R. N. Barnett, in *Nonlinear Phenomena of Phase Transitions and Instabilities,* edited by T. Riste (Plenum, New York, 1982), p. 379.

[18] C. L. Cleveland, U. Landman, and R. N. Barnett, Phys. Rev. Lett. **49**, 790 (1982).

[19] U. Landman, R. N. Barnett, C. L. Cleveland, and R. H. Rast, J. Vac. Sci. Technol. A **3**, 1574 (1985).

[20] J. Q. Broughton, G. H. Gilmer, and K. A. Jackson, Phys. Rev. Lett. **49**, 1496 (1982).

[21] See references in a review by F. F. Abraham, J. Vac. Sci. Technol. B **2**, 534 (1984); see articles in *Fluid Interfacial Phenomena,* edited by C. A. Croxton (Wiley, Chichester, 1986); U. Landman, R. N. Barnett, C. L. Cleveland, W. D. Luedtke, M. W. Ribarsky, D. Scharf, and J. Jortner, Mater. Res. Soc. Symp. Proc. **63**, 273 (1985).

[22] U. Landman, W. D. Luedtke, R. N. Barnett, C. L. Cleveland, M. W. Ribarsky, E. Arnold, S. Ramesh, H. Baumgart, A. Martinez, and B. Khan, Phys. Rev. Lett. **56**, 155 (1986).

[23] F. F. Abraham and J. Q. Broughton, Phys. Rev. Lett. **56**, 734 (1986).

[24] F. H. Stillinger and T. A. Weber, Phys. Rev. B **31**, 5262 (1985).